



CHORUS

This is the accepted manuscript made available via CHORUS. The article has been published as:

High figure of merit magneto-optics from interfacial skyrmions on topological insulators

Tonmoy K. Bhowmick, Amrit De, and Roger K. Lake

Phys. Rev. B **98**, 024424 — Published 25 July 2018

DOI: [10.1103/PhysRevB.98.024424](https://doi.org/10.1103/PhysRevB.98.024424)

High Figure of Merit Magneto Optics from Interfacial Skyrmions on Topological Insulators

Tonmoy K. Bhowmick,^{1,*} Amrit De,^{1,†} and Roger K. Lake^{1,‡}

¹Department of Electrical Engineering, University of California - Riverside, CA 92521

(Dated: May 9, 2018)

In the Kerr rotation geometry, magneto optic memory devices typically suffer from low figure-of-merit (FOM) and long write times. We show that skyrmions formed at the interface of a thin-film multiferroic and a topological insulator can give rise to high FOM magneto optic Kerr effects (MOKEs). Huge differential MOKE can arise in parts of the phase diagram. Resonance like features in the MOKE spectra arising from the induced low energy TI bandgap, the multiferroic-film thickness, and the high energy Drude like behavior are resolved and explained. The Fermi level dependence of the MOKE signatures is distinct for the different magnetic textures. This has broad implications for magnetic texture characterization, electro-optic modulators and isolators and high density magnetic optic memory.

PACS numbers:

Magneto-optic (MO) phenomenon such as Kerr and Faraday rotations, Voigt effect, magneto-plasma reflections and cyclotron resonances arise from broken time reversal symmetry. Some MO effects also arise from the electronic structure's topology, and hence are used to study quantum hall effects¹, Kerr rotations in topological insulators (TIs)^{2,3}, magneto-electric optical effects^{4,5}, magneto-chiral effects⁶, and skyrmions and their Hall effects⁷⁻⁹.

The magneto optic Kerr effect (MOKE) in the polar configuration is particularly interesting due to its application in optical reading-out of magnetically stored information¹⁰⁻¹². A MOKE device can be characterized by its figure-of-merit (FOM)¹³⁻¹⁵, which usually depends on the Kerr rotation angle and the reflectivity. Typically, during the MO memory write process, a focussed laser heats the magnetic material to its Curie temperature, which allows the local magnetic polarization to be flipped. However, the thermally-assisted write processes can be relatively slow. For readout, the Kerr rotation is barely one degree for most MO recording materials¹⁶⁻¹⁹, which can result in higher readout error rates. The Kerr rotation can be enhanced by the use of cavity like resonance conditions, but this usually lowers the reflectivity and makes the memory write process difficult. The required magnetic fields and effective cyclotron frequencies for generating large Kerr rotations in a semi-infinite medium can be unreasonably large^{20,21}. However, skyrmions can give rise to very high emergent fields. The emergent magnetic fields from a periodic lattice of skyrmions (SkX) can reach up to 4000 Tesla, which is two orders of magnitude larger than what can be generated in laboratories.

Skyrmions are topological particle-like configurations of continuous vector fields and are regarded as analogs of magnetic monopoles as each skyrmion is associated with a quantized magnetic flux^{22,23}. Their non-trivial topology is a result of competing Dzyaloshinskii-Moriya (DM), Heisenberg- and Zeeman-interactions^{9,24,25}. In addition, Skyrmions represent a new type of magnetic order^{26,27}, and they have been observed in B20 compounds such as MnSi^{28,29}, FeCoSi³⁰, FeGe³¹ and in Cu₂OSeO₃ which is a multiferroic³². Skyrmions have been proposed for use in novel high density electrically controllable racetrack memories^{33,34}.

The use of magnetic³⁵ and electric fields³⁶ has been pro-

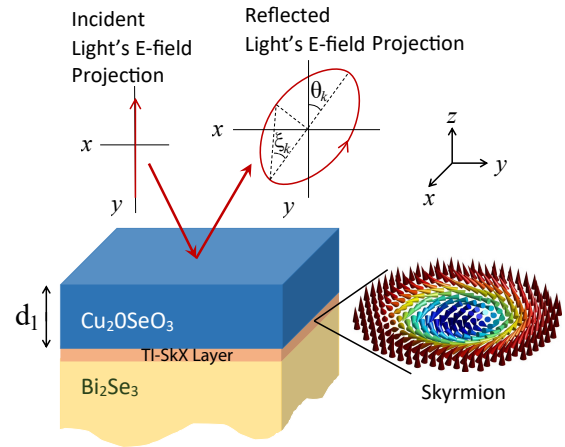


Figure 1: MOKE arising from a magneto-optic device with a thin-film B20 material deposited on top of a semi-infinite TI. A SkX exists at the interface of the TI and B20 compound.

posed to switch between the topologically nontrivial skyrmion spin texture and the topologically trivial ferromagnetic spin texture. Experimentally it is possible to create and erase individual skyrmions using spin polarized currents³⁷. Also magnetic skyrmions can be electrically created on a thin-film of a chiral-lattice magnetic insulator within a few nanoseconds by applying an electric field which couples to the non-collinear skyrmion spins³⁸⁻⁴⁴. In Cu₂OSeO₃, the noncollinear skyrmion spin structure in the host material behaves like a multiferroic due to spin-orbit coupling. This enables skyrmion manipulation via electric fields instead of electric currents^{45,46} or heat pulses⁴⁷. More recently it has been shown that one can reversibly switch between topologically inequivalent ferromagnetic phases and skyrmion phases using electric fields⁴⁸. A topological charge analysis of skyrmion dynamics, energetics, creation, and stability was recently described⁴⁹.

Skyrmions combined with other topological materials can lead to emergent functionalities. In this paper, we show that a skyrmion lattice at the interface of a thin-film B20 compound (such as Cu₂OSeO₃) and a semi-infinite TI (e.g. Bi₂Se₃) gives rise to a high FOM-MOKE (see Fig. 1). The large MOKE

can be exploited for characterization of the spin texture, or application in a magneto–optic memory device.

Skyrmions can form on a TI’s surface⁵⁰ and can become charged⁵¹. The B20–TI heterostructure provides electric field switching of the skyrmion spin texture and a large MOKE from the skyrmion phase. The large differential MOKE leads to fast and high fidelity magneto–optical bit readout. Electric field switching provides fast, low–power writing. The emergent properties of the B20–TI heterostructure provide the physical mechanisms for facile reading and writing of information bits in a topological magneto-optic memory.

For simplicity we consider a device geometry where a semi-infinite TI is capped by a thin Cu_2OSeO_3 layer as shown in Fig. 1. We consider interfaces with a ferromagnetic (FM) texture along with Néel- and Bloch type skyrmions. This simple geometry allows us to best highlight the main MOKE spectral features manifesting from different physical effects. These are: the low energy topological MOKE, thin-film induced enhancement of MOKE and MOKE occurring at the high energy plasma frequency.

Model and Method: We begin by constructing a model where the surface of the TI is coupled to the background spin texture of a SkX. A low energy effective model describing the surface state of Bi_2Se_3 is used where the surface state consists of a single Dirac cone at the Γ point⁵².

We consider the low energy effective Hamiltonian⁵³ describing the decoupled top and bottom surface states of a TI. To avoid the well known Fermion doubling problem on discrete tight-binding lattice, we have added a $k^2\sigma_z$ term to the Hamiltonian of TI^{54,55}

$$H = \hbar v_F(k_x\sigma_y - k_y\sigma_x) - \zeta\hbar v_F(k_x^2 + k_y^2)\sigma_z, \quad (1)$$

where the Fermi velocity v_F , is a material constant. This momentum space Hamiltonian can be transformed into the following real space tight binding Hamiltonian coupled to the Skx spin texture on a rectangular lattice

$$H = \sum_i c_i^\dagger \epsilon c_i - \sum_{\langle i,j \rangle} (c_i^\dagger t c_j + h.c.) - J_H \sum_i c_i^\dagger \boldsymbol{\sigma}_i \cdot \mathbf{S}_i c_i \quad (2)$$

where \mathbf{S}_i is the localized spin of the skyrmion on site i which couples to the TI through the Hund’s rule coupling constant J_H . Here t is the nearest neighbor hopping along the x and y directions, $\boldsymbol{\sigma}_i$ is the spin of the itinerant electron, and ϵ is the on site potential. Periodic boundary conditions are imposed along both the x and y directed edges of a square unit cell consisting of 9×9 lattice sites. We define two dimensionless parameters $t_1 = \hbar v_F/2a$ and $t_2 = \zeta/a$. Here, $\epsilon = 8t_1t_2\sigma_z$, $t_x = -it_1\sigma_y - 2t_1t_2\sigma_z$, $t_y = it_1\sigma_x - 2t_1t_2\sigma_z$. For our numerical simulations we choose the discretization length $a = 15\text{\AA}$, $\zeta = 5\text{\AA}$, $v_F = 0.5 \times 10^6$ m/s and $J_H = 40$ meV.⁵⁰ The interplay between $t_{x,y}$ and J_H dictates the anomalous Hall conductivity of the TI surface in this model.

The magnetization of a single skyrmion can be described by

$$\mathbf{n}(\mathbf{r}) = [\sin \vartheta(r) \cos \varphi(\phi), \sin \vartheta(r) \sin \varphi(\phi), \cos \vartheta(r)], \quad (3)$$

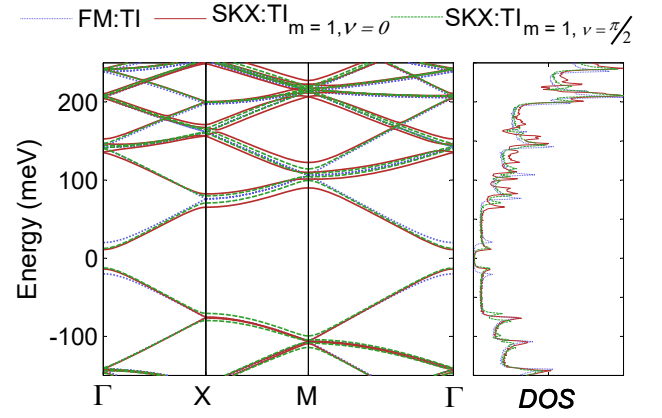


Figure 2: Electronic bandstructure and density of states for proximity coupled FM:TI system and SkX:TI with $m = 1$, and $\nu = 0$ and $\nu = \pi/2$

where $\vartheta(r = 0) = 0$, $\vartheta(0 < r < R_s) = \pi(1 - \frac{r}{R_s})$ and $\vartheta(r > R_s) = \pi$.⁵⁶ $\varphi(\phi) = m\phi + \nu$ and $\phi = \tan^{-1}[y/x]$ where the helicity of the skyrmion is defined by the phase ν .⁵⁷ In this paper, we consider both Néel type ($m = 1, \nu = 0$) and Bloch type skyrmions ($m = 1, \nu = \pi/2$). The skyrmion is centered in the unit cell, and the magnetization $\mathbf{n}(\mathbf{r})$ is evaluated at each lattice site i to obtain \mathbf{S}_i in Eq. (2).

The z -component of $\mathbf{n}(\mathbf{r})$ acts on the electron like position dependent Dirac mass, while the in-plane components can give rise to an emergent gauge field. The total magnetic flux enclosed in a unit skyrmion cell is one flux quantum, $\Phi_0 = h/e$, independent of the skyrmion radius, R_s .⁵⁸ The effective magnetic field is $B_{\text{eff}} = -\Phi_0/(4R_s^2)$.⁵⁹

Electronic Structure: The numerically calculated band structure and the corresponding density of states (DOS) are shown in Fig. 2 for the magnetic textures proximity coupled to the TI. This includes the ferromagnetic case (FM:TI), the Néel type skyrmion ($m = 1, \nu = 0$), and the Bloch type skyrmion ($m = 1, \nu = \pi/2$) proximity coupled to the TI’s surface state. The energy gap at Γ resulting from proximity coupling to the Néel and Bloch type skyrmions is less than the gap resulting from proximity coupling to the FM state. This can be understood from the fact that the skyrmion creates a hole in the background FM texture that reduces the total \hat{z} component of the magnetic moment. The presence of the skyrmions also breaks the degeneracy in other higher energy regions of the spectrum.

Dielectric Tensor Components: Observables such as magneto optic effects and quantum Hall type phenomenon manifest themselves through the dielectric tensor components which depend on the electronic structure and topological properties. In the case of normal optical incidence for an SkX on a TI, the magnetization is along z , which is perpendicular to the surface and parallel to the direction of light propagation, similar to the polar Kerr effect. The x and y directions preserve in-plane symmetry. The complex 3×3 dielectric tensor has diagonal $[\epsilon_{xx}, \epsilon_{yy}, \epsilon_{zz}]$ terms and the off-diagonal ϵ_{xy} terms which are topology dependent.

The matrix elements of the optical conductivity tensor can

be obtained from the band structure calculations using the

Kubo formula^{60,61} as follows:

$$\sigma_{ij} = \frac{ie^2}{(2\pi L)^2 \hbar} \int \frac{d\mathbf{k}}{2\pi} \sum_{n,l} \frac{f_{nl}(\mathbf{k})}{\omega_{nl}(\mathbf{k})} \left(\frac{\Pi(\mathbf{k})_{nl}^i \Pi(\mathbf{k})_{ln}^j}{\omega_{nl}(\mathbf{k}) - \omega + i\gamma} + \frac{\Pi(\mathbf{k})_{ln}^i \Pi(\mathbf{k})_{nl}^j}{\omega_{nl}(\mathbf{k}) + \omega + i\gamma} \right) \quad (4)$$

where $\Pi_{nl}^i(\mathbf{k}) = \langle \psi_n(\mathbf{k}) | v_i | \psi_l(\mathbf{k}) \rangle$ is the velocity operator. Here $\{i, j\} \in \{x, y\}$, γ is a broadening parameter and $\hbar\omega_{nl}(\mathbf{k}) = E_n(\mathbf{k}) - E_l(\mathbf{k})$, is the energy difference of an optical transition between an unoccupied band, n and an occupied band, l . $f_{nl}(\mathbf{k}) = f_n(\mathbf{k}) - f_l(\mathbf{k})$, where $f_n(\mathbf{k})$ is the Fermi filling factor.

Since we are using an effective Hamiltonian to obtain σ_{ij} , we compensate for the missing higher band contributions in Eq. (4) by adding a $\kappa/(\omega + i\gamma)$ term while relating the optical dielectric tensor to the conductivity tensor.

$$\epsilon_{ij}(\omega) = \epsilon_o \delta_{ij} - \frac{4\pi i}{\omega} \sigma_{ij} - \frac{\kappa}{\omega + i\gamma} \quad (5)$$

Here κ is adjusted so that the relative zero frequency dielectric constant ϵ_0 matches the known experimental value. ϵ_o is the vacuum permittivity. For Bi_2Se_3 , $\epsilon(\omega)$ is given by Lorentz oscillator fits to experiment⁶², which in the low energy regime (0–30 meV) is essentially a constant. In the effective surface model, the bulk band contributions to the momentum matrix elements in $\epsilon_{ij}(\omega)$ are not included. However, this does not change the qualitative behavior of the effects shown in this paper, since the calculated $\epsilon_{ij}(\omega)$ s are qualitatively similar to experiment⁶². Therefore we argue that all the higher energy MOKE features discussed in this paper would still be seen in experiments, but at higher optical frequencies.

The dielectric function consists of Berry connection type terms, $a_i(\mathbf{k}) = -i \langle \psi(\mathbf{k}) | \nabla_i | \psi(\mathbf{k}) \rangle$, which behave like a fictitious momentum space gauge potential or an equivalent magnetic field $b_z(\mathbf{k}) = \partial_{k_x} a_y(\mathbf{k}) - \partial_{k_y} a_x(\mathbf{k})$. The MOKE can therefore be viewed as an optical manifestation of the Berry curvature via the ϵ_{xy} term. This is similar to charge transport, where the xy response is proportional to the Chern number^{26,63–65}, which is the integral of Berry curvature over the first Brillouin zone, $\mathcal{C} = \frac{1}{2\pi} \int d^2k b_z(\mathbf{k})$. There are differences between MOKE and quantum Hall effect type topological manifestations due to conduction \leftrightarrow valance transitions and the frequency dependence in optics. ϵ_{xy} depends on the topological charge across a gap. Usually ϵ_{xy} is much smaller than the diagonal ϵ_{xx} . In our case the three different magnetic textures result in the same Chern number across the fundamental gap of the proximity induced magnetic TI surface state, so that ϵ_{xy} does not vary much when the Fermi energy is set to 0.

Magneto-Optics: The complex in-plane index of refraction is $n_{\pm} = \sqrt{\epsilon_{\pm}} = \sqrt{\epsilon_{xx} \pm i\epsilon_{xy}}$ where, the $+$ ($-$) signs represents right(left) circularly polarized (RCP(LCP)) light propagation. The complex MOKE effect is expressed as: $\Theta_k = \theta_k + i\xi_k$ where the Kerr rotation and ellipticity are,

respectively

$$\theta_k = (\Delta_+ - \Delta_-)/2 \quad (6)$$

$$\xi_k = (|r_+| - |r_-|)/(|r_+| + |r_-|). \quad (7)$$

Since the eigen-modes here are LCP and RCP, the Kerr rotation angle can be expressed as the phase difference between these two modes. The complex phase Δ_{\pm} can be obtained from the Fresnel reflection coefficients r_{\pm} .

The MOKE arising because of the thin-film structure can be significantly altered by internal reflection at various interfaces of the layers. A 2×2 characteristic matrix method can be used to characterize the MOKE spectra of a multilayer structure at normal incidence, assuming that the materials are homogeneous and isotropic. The transfer matrices are in the LCP/RCP eigenmode basis, which for N parallel layers is:

$$\mathbf{S}^{\pm} = \prod_{j=0}^N \frac{1}{t_{j,j+1}^{\pm}} \begin{bmatrix} r_{j,j+1}^{\pm} & 1 \\ 1 & r_{j,j+1}^{\pm} \end{bmatrix} \begin{bmatrix} e^{i\beta_{j+1}^{\pm}} & 0 \\ 0 & e^{-i\beta_{j+1}^{\pm}} \end{bmatrix} \quad (8)$$

The Fresnel reflection and transmission coefficients at normal incidence for each interface are respectively given by: $r_{j,j+1}^{\pm} = (n_j^{\pm} - n_{j+1}^{\pm})/(n_j^{\pm} + n_{j+1}^{\pm})$ and $t_{j,j+1}^{\pm} = (2n_j^{\pm})/(n_j^{\pm} + n_{j+1}^{\pm})$. The phase factor is given by $\beta_j = (2\pi/\lambda)n_j d_j$, where d_j is the thickness of the j^{th} layer and λ is the optical wavelength. The complex reflection coefficient from the resultant characteristic transfer matrix is: $r^{\pm} = S_{12}^{\pm}/S_{11}^{\pm} = |r^{\pm}| \exp(-i\Delta_{\pm})$ where $S_{ij}^{\pm} \in \mathbf{S}^{\pm}$. The observed reflective intensity is $R_{\pm} = |r_{\pm}|^2$.

Discussion: We first consider only an ideal single interface for our initial analysis. The MOKE spectra and reflectivity and the optical dielectric function are shown for a Néel type skyrmion ($m = 1, \nu = 0$) on a TI in Fig. 3 for illustration. The corresponding spectra for FM:TI and Bloch type skyrmion ($m = 1, \nu = \pi/2$) on a TI look very similar.

Two distinct resonance like features can be seen for the Kerr rotation and the ellipticity. From the approximation⁶⁶: $\Theta_k \approx [n_+ - n_-]/[n_+ n_- - 1]$, it is easy to see that MOKE resonances spectrally occurs whenever $\epsilon_+ \epsilon_- \sim 1$ ²⁰. In Fig. 3, one MOKE resonance is in the low energy regime and occurs at 38 meV. This is close to the size of the fundamental gap that the magnetic texture (Néel type skyrmion in this case) induces in the TI. We will explore this regime, where the quantization effects occurs, in more detail later in this paper.

The high energy MOKE resonance features occur in the energy regime where free electron like behavior dominates. Hence this can be qualitatively understood from the semiclas-

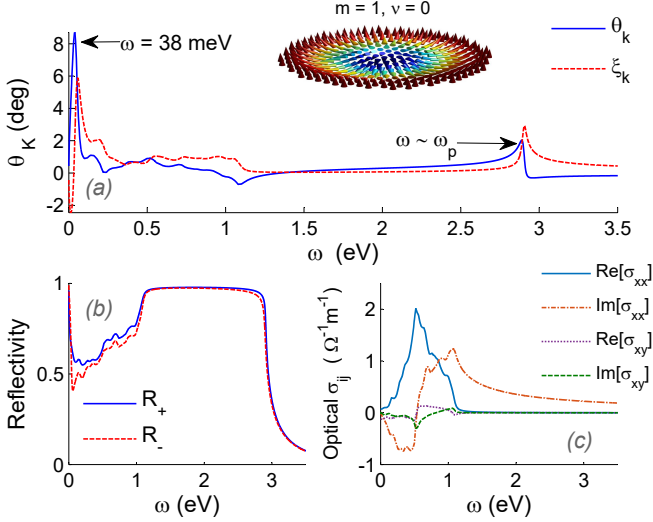


Figure 3: (a) Kerr rotation and ellipticity for a single SkX:TI interface for Néel type skyrmion $m = 1, \nu = 0$ (b) Reflectivity for left- and right-circularly-polarized light. (c) The corresponding optical conductivity of SkX:TI system

sical Drude model: $\epsilon_{\pm} \propto (1 - \omega_p^2 / [\omega(\omega \pm \omega_c + i\gamma)])$, where ω_p is the plasma frequency and ω_c is the cyclotron frequency.

If $\epsilon_{xy} \ll \epsilon_{xx}$ ⁶⁶, an additional approximation can be made for the Kerr rotation, $\Theta_k \approx \epsilon_{xy} / (1 - \epsilon_{xx}) \sqrt{\epsilon_{xx}}$. From this most commonly used expression for calculating MOKE, it can be seen that MOKE resonances should occur when $\epsilon_{xx} = 1$. This is also where R_{\pm} goes to zero and the MOKE resonance occurs near $\omega = \omega_p$ ⁶⁷⁻⁶⁹. Note that similarly, magneto-plasmons in graphene give large magneto optic effects^{70,71}. Using the Drude model, one can derive a simple expression for the spectral occurrence of this MOKE resonance²⁰

$$\omega_{\pm} \approx \frac{1}{2} \left(\gamma + \sqrt{\omega_c^2 - \gamma^2 + 4\omega_p^2 \pm \omega_c} \right) \quad (9)$$

In an attempt to explain the high energy spectral features using the Drude model, we extract the effective ω_p and effective ω_c using the optical sum rules:

$$\int_0^{\infty} \omega \text{Im}[\epsilon_{xx}(\omega)] d\omega = \frac{\pi}{2} \omega_p^2 \quad (10)$$

$$\int_0^{\infty} \omega^2 \text{Re}[\epsilon_{xy}(\omega)] d\omega = -\frac{\pi}{2} \omega_p^2 \omega_c \quad (11)$$

These values can be substituted into Eq. (9) to obtain ω_{\pm} , which is listed in Table I along with other parameters. The analytically obtained ω_{+} is in excellent agreement with ω_{θ} – which is the frequency at which the high energy MOKE resonance occurs. In this high energy regime, the magnitude of $\theta_k^{max} \propto \omega_c \omega_p^2 \propto \epsilon_{xy}$ as shown in Table I. Overall if $\omega_c \ll \omega_p$ then the Kerr rotation resonance is at $\omega \approx \omega_p$. Whereas if $\omega_c \gtrsim \omega_p$ then a large MOKE resonance edge split occurs at frequencies determined by $\epsilon_{+}\epsilon_{-} \approx 1$ ²⁰. Note that these calculations are for a single interface (i.e. assuming both the Cu_2OSeO_3 and Bi_2Se_3 layers are semi-infinite).

Spin Texture	$\theta_k^{\omega_p}$	ω_p (eV)	ω_c (eV)	ω_{θ} (eV)	ω_{+} (eV)
FM	2.175	2.822	0.014	2.894	2.878
$m = 1, \nu = 0$	2.032	2.816	0.013	2.888	2.872
$m = 1, \nu = \pi/2$	2.029	2.816	0.013	2.889	2.872

Table I: List of high energy (> 2 eV) Kerr rotation angles and related parameters due to free electron like behavior for various magnetic textures on TI. Maximum Kerr rotation angle $\theta_k^{\omega_p}$, effective plasma frequency ω_p , cyclotron frequency ω_c , frequency of maximum Kerr rotation ω_{θ} , and its predicted value ω_{+} .

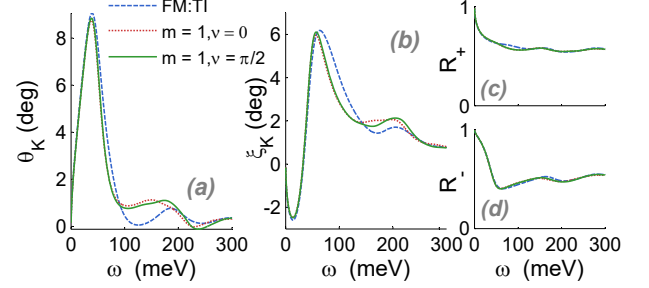


Figure 4: A comparison of the (a) Kerr rotation, (b) ellipticity, (c) RCP reflectivity, and (d) LCP reflectivity for FM:TI and SkX:TI with $m = 1, \nu = 0$ and $m = 1, \nu = \pi/2$.

We next consider the MOKE features around 38 meV. The MOKE spectra is shown in Fig. 4 in the energy regime below 300 meV. The maximum Kerr rotation is about 9° , which occurs when R_{\pm} are the furthest apart as this increases $\Delta_{+} - \Delta_{-}$. The Kerr rotation is sufficiently large for magneto-optic recording applications. In this case, there is not a clear distinguishing feature between the interface with the FM and the interface with the two different skyrmion spin textures. For these calculations, the Fermi Energy, $E_f = 0$. The MOKE spectral features in this energy regime are primarily dominated by the gap in the TI surface state, which is induced by the magnetic textures. The Chern number in the gap is the same for all three magnetic textures, and hence there is no clear distinction in the MOKE features for $E_f = 0$.

MOKE can also be enhanced by the resonance like effects that arise from adjusting the film thickness of different materials. In order to understand the effects of this for our system, we consider a thin-film structure as shown in Fig. 1 where a Cu_2OSeO_3 film of thickness d_1 sits on a semi-infinite Bi_2Se_3 layer. The dispersion relation for Cu_2OSeO_3 was obtained using experimentally fitted Lorentz oscillators⁷². As is typical with multiferroics, there are several low energy phonon modes present in the Cu_2OSeO_3 dielectric function which are also reproduced by the model⁷². We assume that the SkX system exists in a 1 nm thin layer at the interface of the Cu_2OSeO_3 thin film and semi-infinite Bi_2Se_3 layer. The SkX:TI effects manifest themselves via n_{\pm} . The refractive index of air is used for the semi-infinite media above the Cu_2OSeO_3 layer as shown in Fig. 1.

A comparison of the magneto optic Kerr rotation, ellipticity, LCP and RCP reflectivity spectra are shown in Fig. 5 for a

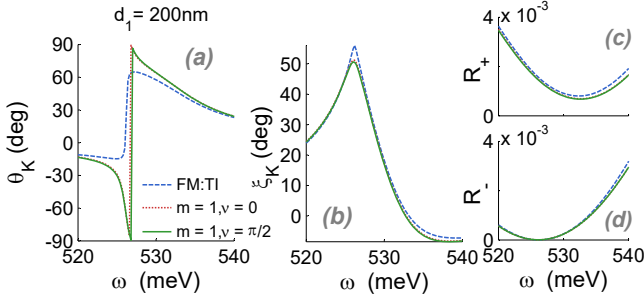


Figure 5: A close-up comparison of the $d_1 = 200$ nm thin-film induced resonances in the (a) Kerr rotation and (b) ellipticity. The corresponding (c) RCP reflectivity and (d) LCP reflectivity is also shown for the FM:TI- and SkX:TI interfaces with Bloch ($m=1$, $\nu = \pi/2$) and Néel ($m=1$, $\nu = 0$) type skyrmions.

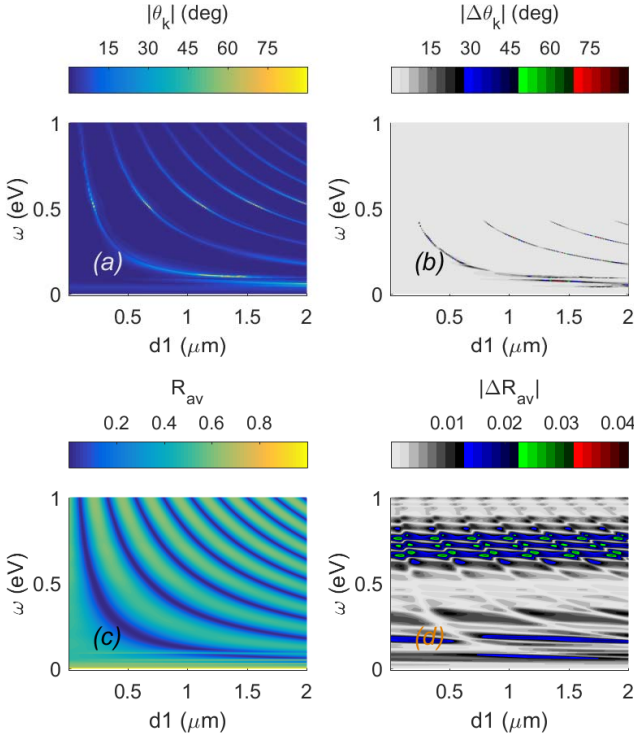


Figure 6: (a) The Kerr rotation for the Néel type ($m = 1$, $\nu = 0$) interface (b) and its Kerr rotation difference with the FM interface, $\Delta\theta_k = \theta_k^{FM:TI} - \theta_k^{SkX:TI}$ as a function of frequency and Cu_2OSeO_3 film thickness d_1 . (c) Average reflectivity $R_{av} = (R_+ + R_-)/2$ for Néel type interface and (d) Difference in the average reflectivity: $\Delta R_{av} = R_{av}^{FM:TI} - R_{av}^{SkX:TI}$

Néel type skyrmion, the Bloch type skyrmion, and the FM:TI for a Cu_2OSeO_3 layer with film thickness $d_1 = 200 \mu\text{m}$. At this particular film thickness, $R_- \rightarrow 0$, which causes a huge Kerr rotation resonance of $\sim 90^\circ$ as the phase difference between LCP and RCP is maximized. Also for a given film thicknesses for the Cu_2OSeO_3 layer, the MOKE spectra can be notably different between the different SkX textures and the FM state. In this example the maximum Kerr rotation arising from the FM:TI is ~ 60 deg and occurs at a different

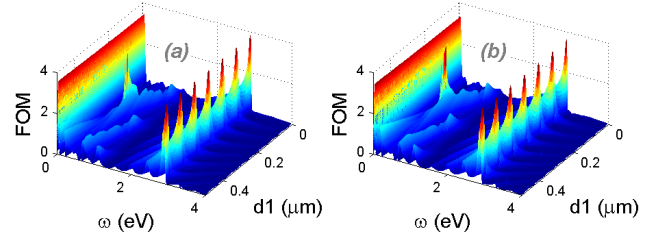


Figure 7: Figure of merit for (a) FM:TI (b) Néel SkX:TI

optical frequency.

In order to achieve low error magneto-optic readouts, the different states should be maximally discernable. We therefore examine the phase diagram, as a function of ω and d_1 , for the differential MOKE effects,

$$\Delta\theta_k = \theta_k^{FM:TI} - \theta_k^{SkX:TI} \quad (12)$$

$$\Delta R_{av} = R_{av}^{FM:TI} - R_{av}^{SkX:TI} \quad (13)$$

where $R_{av} = (R_+ + R_-)/2$ is the average reflectivity. We take $\arctan[\tan(\theta_k)]$ to avoid Kerr rotations greater than ± 90 deg.

The phase diagram for both the Kerr rotation and the average reflectivity is shown in Fig. 6 (a) and (c) for the Néel type skyrmion. Both Néel- and Bloch-type skyrmions have identical phase diagrams where θ_k and R_{av} vary periodically with ω and d_1 . There are several periodic parts of this phase diagram that are insensitive to errors in film-thickness or spectral tuning. By tuning d_1 a large Kerr rotation can be obtained for any frequency $\gtrsim 100$ meV. The reflectivity would, however, be low in this case when θ_k is maximized. The differential $\Delta\theta_k$ and ΔR_{av} effects are shown in Fig. 6 (b) and (d), respectively. Generally ΔR_{av} is low. The FM:TI and SkX:TI have slightly different periodicity. Therefore the differential Kerr rotation can reach up to $\pm 90^\circ$ depending on d_1 . The phase diagram also suggests that either the Néel- or Bloch-type skyrmions could be used for such a magneto-optic recording device.

Typically, large Kerr rotations are accompanied by low reflectivities which reduces the effectiveness of a MO device. The overall useful MO signal can be quantified by the figure of merit (FOM)¹³⁻¹⁵ for the Kerr rotation configuration, defined here as,

$$FOM = |\theta_k| \times \max(|r_+|, |r_-|). \quad (14)$$

This can be used to characterize MO memory and other MO devices such as modulators and isolators.

For our device, the FOM is shown in Fig. 7 as a function of ω and d_1 . At $\omega \approx \omega_p \approx 2.8$ eV, the FOM peaks, arising from the free electron behavior, periodically as a function of d_1 . The FOM resonance at $\omega \approx 0.52$ eV, and $d_1 = 0.2 \mu\text{m}$ is due to the features shown in Fig. 5. Even though $\theta_k \sim 90^\circ$, the FOM is not the highest due to low R_\pm . The FOM peak here is higher for the Néel SkX:TI than it is for the FM:TI. Also note that the Néel and Bloch SkX:TI's FOM are identical.

Finally, the most fascinating result is that the FOM at $\omega \approx 38$ meV is independent of d_1 . This is an encouraging result for

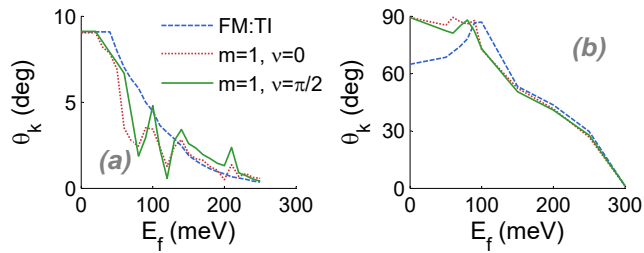


Figure 8: (a) Low energy spectral regime Kerr rotation, θ_k , as a function of Fermi energy, E_f , calculated around $\omega \sim 38$ meV, which is where θ_k^{max} occurs in Fig. 4 at $E_f = 0$. (b) Thin-film thickness ($d_1 = 200$ nm) induced Kerr rotation in the intermediate spectral regime, as a function of Fermi energy. Kerr rotations are calculated around $\omega \sim 520$ meV, which is where θ_k^{max} occurs for $E_f = 0$ in Fig. 5.

experiments and for devices as this implies that the MO-FOM is independent of any error in the Cu_2OSeO_3 film-thickness. Also, this FOM at the gap energy is also the highest in the entire FOM phase diagram.

Finally, we study electro-optic switching effects as a function of Fermi energy. In Fig. 8(a), θ_k is shown as a function of Fermi energy E_f . All values are shown at the ω at which θ_k^{max} occurs for $E_f = 0$ in the low energy regime (see Fig. 4). Similarly Fig. 8(b), θ_k is shown as a function of E_f in the intermediate energy regime. Here ω for each magnetic texture is where the resonances induced by the Cu_2OSeO_3 film thickness occur in Fig. 5(a).

In Fig. 8(a), all three textures show distinct behavior. While θ_k^{max} for the FM:TI shows a monotonic decrease with increasing E_f , the Néel type and Bloch type SkXs show somewhat oscillatory non-monotonic behavior. This can be explained as follows. In the present model for the FM:TI all the states above the gap are degenerate and free electron like. Hence θ_k decreases monotonically with E_f . Whereas in case of the SkX:TI, the states just above the gap are non-degenerate and the bands are split. This leads to additional peaks and valleys in the DOS, which causes the sudden jumps in Fig. 8(a) as

E_f moves up in energy. Lastly θ_k as a function of E_f differs for the Néel type and Bloch type SkXs because their density of states is different above the gap as shown in Fig. 2. These effects can be numerically heightened if J_H is increased ten-fold. The band-splittings in Fig. 2 for the two SkXs, then evolve into energy gaps where the SkXs have different Chern numbers in the gaps. This will lead to very distinct MOKE signatures as a function of E_f .

These E_f dependent non-monotonic θ_k effects are not seen in Fig. 8(b), where the MOKE resonances are induced by the Cu_2OSeO_3 thin-film. Here, the Néel type and Bloch type SkXs are indistinguishable, but they both differ from the FM:TI. θ_k at $E_f = 0$ is much smaller for the FM:TI because $d_1 = 200$ nm is not optimal in this case. The FM:TI and SkX:TI show distinct differences only for low E_f .

In summary, the MOKE from SkX-hosting thin-film B20 type compounds interfaced with TI structures displays rich physics with important device applications. High FOM is obtained from the low energy topological MOKE, the thin-film induced enhancement of MOKE, and the MOKE occurring at the high energy plasma frequency. The MOKE-FOM phase diagram shows that the low energy peaks below the TI's bulk energy gap are large and independent of d_1 . For the thin-film induced resonance, the differential MOKE can be large for the FM and SkX states, which is useful for device applications. As E_f is swept above the exchange gap of the surface state, θ_k decreases monotonically for FM:TIs, and it is distinctly oscillatory and non-monotonic for SkX:TIs. These distinguishing $\theta_k(E_f)$ features are not seen for the thin-film induced MOKE resonance. With a large FOM, optical readout can lead to high density and high fidelity MO memory devices and electro-optic devices such as modulators and optical-isolators^{73,74}.

Acknowledgement: This work was supported by the NSF ECCS-1408168 Physical Mechanisms and Limits of Skyrmions for Information Processing and Storage and as part of the Spins and Heat in Nanoscale Electronic Systems (SHINES) an Energy Frontier Research Center funded by the U.S. Department of Energy, Office of Science, Basic Energy Sciences under Award #DE-SC0012670.

* tchow001@ucr.edu, These authors contributed equally

† amritde@gmail.com, These authors contributed equally

‡ rlake@ece.ucr.edu

¹ I. Kukushkin and V. Timofeev, *Advances in Physics* **45**, 147 (1996).

² W.-K. Tse and A. H. MacDonald, *Phys. Rev. Lett.* **105**, 057401 (2010).

³ W.-K. Tse and A. H. MacDonald, *Phys. Rev. B* **84**, 205327 (2011).

⁴ T. Arima, *Journal of Physics: Condensed Matter* **20**, 434211 (2008).

⁵ E. Atmatzakis, N. Papanikolaou, V. Fedotov, G. Vienne, and N. I. Zheludev, *Nanophotonics* **7**, 199 (2018).

⁶ R. Sessoli, M.-E. Boulon, A. Caneschi, M. Mannini, L. Poggini, F. Wilhelm, and A. Rogalev, *Nature physics* **11**, 69 (2015).

⁷ M. Vomir, R. Turnbull, I. Birced, P. Parreira, D. A. MacLaren, S. L. Lee, P. Andre, and J.-Y. Bigot, *Nano letters* **16**, 5291 (2016).

⁸ S. Woo, K. M. Song, X. Zhang, Y. Zhou, M. Ezawa, X. Liu, S. Finizio, J. Raabe, N. J. Lee, S.-I. Kim, et al., *Nature Communications* **9**, 959 (2018).

⁹ W. Jiang, X. Zhang, G. Yu, W. Zhang, X. Wang, M. B. Jungfleisch, J. E. Pearson, X. Cheng, O. Heinonen, K. L. Wang, et al., *Nature Physics* **13**, 162 (2017).

¹⁰ P. Hansen, *Journal of Magnetism and Magnetic Materials* **83**, 6 (1990).

¹¹ Y. Suzuki, T. Katayama, S. Yoshida, K. Tanaka, and K. Sato, *Phys. Rev. Lett.* **68**, 3355 (1992).

¹² M. MANSURIPUR, *Opt. Photon. News* **11**, 34 (2000), URL <http://www.osa-opn.org/abstract.cfm?URI=opn-11-10-34>.

¹³ M. Mansuripur, *Applied physics letters* **49**, 19 (1986).

¹⁴ W. A. Challener, *Journal of Physics and Chemistry of Solids* **56**, 1499 (1995), ISSN 0022-3697, proceedings of the 1994 Confer-

- ence on Magneto-optic Materials.
- ¹⁵ A. R. Taussig, G. F. Dionne, and C. A. Ross, *Phys. Rev. B* **77**, 012407 (2008).
 - ¹⁶ B. Lairson and B. Clemens, *Applied physics letters* **63**, 1438 (1993).
 - ¹⁷ P. Van Engen, K. Buschow, R. Jongebreur, and M. Erman, *Applied Physics Letters* **42**, 202 (1983).
 - ¹⁸ K. Egashira and T. Yamada, *Journal of Applied Physics* **45**, 3643 (1974).
 - ¹⁹ W. Reim and D. Weller, *Applied physics letters* **53**, 2453 (1988).
 - ²⁰ A. De and A. Puri, *Journal of Applied Physics* **92**, 5401 (2002).
 - ²¹ A. De and A. Puri, *Journal of Applied Physics* **93**, 1120 (2003).
 - ²² I. Gross, W. Akhtar, A. Hrabec, J. Sampaio, L. Martínez, S. Chouaieb, B. Shields, P. Maletinsky, A. Thiaville, S. Rohart, et al., *Physical Review Materials* **2**, 024406 (2018).
 - ²³ J. Li, A. Tan, K. Moon, A. Doran, M. Marcus, A. Young, E. Arenholz, S. Ma, R. Yang, C. Hwang, et al., *Nature communications* **5**, 4704 (2014).
 - ²⁴ R. Tolley, S. Montoya, and E. Fullerton, *Physical Review Materials* **2**, 044404 (2018).
 - ²⁵ S. Luo, M. Song, X. Li, Y. Zhang, J. Hong, X. Yang, X. Zou, N. Xu, and L. You, *Nano letters* (2018).
 - ²⁶ U. Röbller, A. Bogdanov, and C. Pfeleiderer, *Nature* **442**, 797 (2006).
 - ²⁷ S. Mühlbauer, B. Binz, F. Jonietz, C. Pfeleiderer, A. Rosch, A. Neubauer, R. Georgii, and P. Böni, *Science* **323**, 915 (2009).
 - ²⁸ A. Tonomura, X. Yu, K. Yanagisawa, T. Matsuda, Y. Onose, N. Kanazawa, H. S. Park, and Y. Tokura, *Nano letters* **12**, 1673 (2012).
 - ²⁹ X. Yu, J. P. DeGrave, Y. Hara, T. Hara, S. Jin, and Y. Tokura, *Nano letters* **13**, 3755 (2013).
 - ³⁰ X. Yu, Y. Onose, N. Kanazawa, J. Park, J. Han, Y. Matsui, N. Nagaosa, and Y. Tokura, *Nature* **465**, 901 (2010).
 - ³¹ S. Huang and C. Chien, *Physical review letters* **108**, 267201 (2012).
 - ³² S. Seki, X. Yu, S. Ishiwata, and Y. Tokura, *Science* **336**, 198 (2012).
 - ³³ D. Zhu, W. Kang, S. Li, Y. Huang, X. Zhang, Y. Zhou, and W. Zhao, *IEEE Transactions on Electron Devices* **65**, 87 (2018).
 - ³⁴ G. Yu, P. Upadhyaya, X. Li, W. Li, S. K. Kim, Y. Fan, K. L. Wong, Y. Tserkovnyak, P. K. Amiri, and K. L. Wang, *Nano letters* **16**, 1981 (2016).
 - ³⁵ M. Mochizuki, *Phys. Rev. Lett.* **108**, 017601 (2012).
 - ³⁶ M. Mochizuki and Y. Watanabe, *Applied Physics Letters* **107**, 082409 (2015).
 - ³⁷ N. Romming, C. Hanneken, M. Menzel, J. E. Bickel, B. Wolter, K. von Bergmann, A. Kubetzka, and R. Wiesendanger, *Science* **341**, 636 (2013).
 - ³⁸ Y. Nakatani, M. Hayashi, S. Kanai, S. Fukami, and H. Ohno, *Applied Physics Letters* **108**, 152403 (2016).
 - ³⁹ J. S. White, I. Levatić, A. Omrani, N. Egetenmeyer, K. Prša, I. Živković, J. Gavilano, J. Kohlbrecher, M. Bartkowiak, H. Berger, et al., *Journal of Physics: Condensed Matter* **24**, 432201 (2012).
 - ⁴⁰ W. Koshibae, Y. Kaneko, J. Iwasaki, M. Kawasaki, Y. Tokura, and N. Nagaosa, *Japanese Journal of Applied Physics* **54**, 053001 (2015).
 - ⁴¹ M. Schott, A. Bernand-Mantel, L. Ranno, S. Pizzini, J. Vogel, H. Béa, C. Baraduc, S. Auffret, G. Gaudin, and D. Givord, *Nano Letters* **17**, 3006 (2017).
 - ⁴² Y. Okamura, F. Kagawa, S. Seki, and Y. Tokura, *Nature communications* **7**, 12669 (2016).
 - ⁴³ M. Mochizuki and Y. Watanabe, *Applied Physics Letters* **107**, 082409 (2015).
 - ⁴⁴ N. Romming, C. Hanneken, M. Menzel, J. E. Bickel, B. Wolter, K. von Bergmann, A. Kubetzka, and R. Wiesendanger, *Science* **341**, 636 (2013).
 - ⁴⁵ K. Everschor, M. Garst, R. Duine, and A. Rosch, *Physical Review B* **84**, 064401 (2011).
 - ⁴⁶ J. Zang, M. Mostovoy, J. H. Han, and N. Nagaosa, *Physical review letters* **107**, 136804 (2011).
 - ⁴⁷ W. Koshibae and N. Nagaosa, *Nature communications* **5**, ncomms6148 (2014).
 - ⁴⁸ P.-J. Hsu, A. Kubetzka, A. Finco, N. Romming, K. von Bergmann, and R. Wiesendanger, *Nature Nanotechnology* **12**, 123 (2016).
 - ⁴⁹ G. Yin, Y. Li, L. Kong, R. K. Lake, C.-L. Chien, and J. Zang, *Physical Review B* **93**, 174403 (2016).
 - ⁵⁰ K. Yasuda, R. Wakatsuki, T. Morimoto, R. Yoshimi, A. Tsukazaki, K. Takahashi, M. Ezawa, M. Kawasaki, N. Nagaosa, and Y. Tokura, *Nature Physics* **12**, 555 (2016).
 - ⁵¹ H. M. Hurst, D. K. Efimkin, J. Zang, and V. Galitski, *Physical Review B* **91**, 060401 (2015).
 - ⁵² H.-Z. Lu, W.-Y. Shan, W. Yao, Q. Niu, and S.-Q. Shen, *Physical review B* **81**, 115407 (2010).
 - ⁵³ Y. Xia, D. Qian, D. Hsieh, L. Wray, A. Pal, H. Lin, A. Bansil, D. Grauer, Y. Hor, R. Cava, et al., *Nature Physics* **5**, 398 (2009).
 - ⁵⁴ L. Susskind, *Physical Review D* **16**, 3031 (1977).
 - ⁵⁵ S. Hong, V. Diep, S. Datta, and Y. P. Chen, *Physical Review B* **86**, 085131 (2012).
 - ⁵⁶ J. L. Lado and J. Fernández-Rossier, *Physical Review B* **92**, 115433 (2015).
 - ⁵⁷ N. Nagaosa and Y. Tokura, *Nature nanotechnology* **8**, 899 (2013).
 - ⁵⁸ K. Hamamoto, M. Ezawa, and N. Nagaosa, *Physical Review B* **92**, 115417 (2015).
 - ⁵⁹ N. Kanazawa, M. Kubota, A. Tsukazaki, Y. Kozuka, K. Takahashi, M. Kawasaki, M. Ichikawa, F. Kagawa, and Y. Tokura, *Physical Review B* **91**, 041122 (2015).
 - ⁶⁰ D. Thouless, M. Kohmoto, M. Nightingale, and M. Den Nijs, *Physical Review Letters* **49**, 405 (1982).
 - ⁶¹ M. Kohmoto, *Annals of Physics* **160**, 343 (1985).
 - ⁶² M. Eddrief, F. Vidal, and B. Gallas, *Journal of Physics D: Applied Physics* **49**, 505304 (2016).
 - ⁶³ A. Jackson, A. Jackson, and V. Pasquier, *Nuclear Physics A* **432**, 567 (1985).
 - ⁶⁴ W. Münzer, A. Neubauer, T. Adams, S. Mühlbauer, C. Franz, F. Jonietz, R. Georgii, P. Böni, B. Pedersen, M. Schmidt, et al., *Physical Review B* **81**, 041203 (2010).
 - ⁶⁵ X. Yu, N. Kanazawa, W. Zhang, T. Nagai, T. Hara, K. Kimoto, Y. Matsui, Y. Onose, and Y. Tokura, *Nature communications* **3**, 988 (2012).
 - ⁶⁶ P. N. Argyres, *Phys. Rev.* **97**, 334 (1955).
 - ⁶⁷ H. Feil and C. Haas, *Phys. Rev. Lett.* **58**, 65 (1987).
 - ⁶⁸ A. De and A. Puri, *Journal of Applied Physics* **91**, 9777 (2002).
 - ⁶⁹ M. Abe and T. Suwa, *Phys. Rev. B* **70**, 235103 (2004).
 - ⁷⁰ A. Ferreira, N. M. R. Peres, and A. H. Castro Neto, *Phys. Rev. B* **85**, 205426 (2012).
 - ⁷¹ M. Tymchenko, A. Y. Nikitin, and L. Martin-Moreno, *ACS nano* **7**, 9780 (2013).
 - ⁷² K. H. Miller, X. S. Xu., H. Berger, E. S. Knowles, D. J. Arenas, M. W. Meisel, and D. B. Tanner, *Phys. Rev. B* **82**, 144107 (2010).
 - ⁷³ L. Bi, J. Hu, P. Jiang, H. S. Kim, D. H. Kim, M. C. Onbasli, G. F. Dionne, and C. A. Ross, *Materials* **6**, 5094 (2013), ISSN 1996-1944.
 - ⁷⁴ M. C. Onbasli, L. Beran, M. Zahradník, M. Kučera, R. Antoš, J. Mistrík, G. F. Dionne, M. Veis, and C. A. Ross, *Scientific reports* **6**, 23640 (2016).